Opto-Electronic Science

CN 51-1800/O4 ISSN 2097-0382 (Print) ISSN 2097-4000 (Online)

# Multi-resonance enhanced photothermal synergistic fiber-optic Tamm plasmon polariton tip for high-sensitivity and rapid hydrogen detection

Xinran Wei, Yuzhang Liang, Xuhui Zhang, Rui Li, Haonan Wei, Yijin He, Lanlan Shen, Yurui Fang, Ting Xu and Wei Peng

**Citation:** Wei XR, Liang YZ, Zhang XH, et al. Multi-resonance enhanced photothermal synergistic fiber-optic Tamm plasmon polariton tip for high-sensitivity and rapid hydrogen detection. *Opto-Electron Sci* **4**, 240029 (2025).

https://doi.org/10.29026/oes.2025.240029

Received: 11 November 2024; Accepted: 15 January 2025; Published online: 21 May 2025

## Related articles

**Highly sensitive and stable probe refractometer based on configurable plasmonic resonance with nano-modified fiber core**

Jianying Jing, Kun Liu, Junfeng Jiang, Tianhua Xu, Shuang Wang, Tiegen Liu

*Opto-Electronic Advances* 2023 **6**, 220072 doi: 10.29026/oea.2023.220072

**Three-dimensional multichannel waveguide grating filters**

Si-Yu Yin, Qi Guo, Shan-Ren Liu, Ju-Wei He, Yong-Sen Yu, Zhen-Nan Tian, Qi-Dai Chen

*Opto-Electronic Science* 2024 **3**, 240003 doi: 10.29026/oes.2024.240003

**Direct detection with an optimal transfer function: toward the electrical spectral efficiency of coherent homodyne detection**

Xingfeng Li, Jingchi Li, Xiong Ni, Hudi Liu, Qunbi Zhuge, Haoshuo Chen, William Shieh, Yikai Su

*Opto-Electronic Science* 2025 **4**, 240020 doi: 10.29026/oes.2025.240020

**A highly sensitive LITES sensor based on a multi-pass cell with dense spot pattern and a novel quartz tuning fork with low frequency**

Yahui Liu, Shunda Qiao, Chao Fang, Ying He, Haiyue Sun, Jian Liu, Yufei Ma

*Opto-Electronic Advances* 2024 **7**, 230230 doi: 10.29026/oea.2024.230230

**More related article in Opto-Electronic Journals Group website**

Opto-Electronic Science

Article

xxxx 2025, Vol. 4, No.

DOI: 10.29026/oes.2025.240029 CSTR: 32246.14.oes.2025.240029

# Multi-resonance enhanced photothermal synergistic fiber-optic Tamm plasmon polariton tip for high-sensitivity and rapid hydrogen detection

Xinran Wei[1], Yuzhang Liang[1]*, Xuhui Zhang[2,3], Rui Li[1], Haonan Wei[1], Yijin He[1], Lanlan Shen[1], Yurui Fang[1], Ting Xu[4,5]* and Wei Peng[1]

Accurate and real-time detection of hydrogen ($H_2$) is essential for ensuring energy security. Fiber-optic $H_2$ sensors are gaining attention for their integration and remote sensing capabilities. However, they face challenges, including complex fabrication processes and limited response times. Here, we propose a fiber-optic $H_2$ sensing tip based on Tamm plasmon polariton (TPP) resonance, consisting of a multilayer metal/dielectric Bragg reflector deposited directly on the fiber end facet, simplifying the fabrication process. The fiber-optic TPP (FOTPP) tip exhibits both TPP and multiple Fabry-Perot (FP) resonances simultaneously, with the TPP employed for highly sensitive $H_2$ detection. Compared to FP resonance, TPP exhibits more than twice the sensitivity under the same structural dimension without cavity geometry deformation. The excellent performance is attributed to alterations in phase-matching conditions, driven by changes in penetration depth of TPP. Furthermore, the FP mode is utilized to achieve an efficient photothermal effect to catalyze the reaction between $H_2$ and the FOTPP structure. Consequently, the response and recovery speeds of the FOTPP tip under resonance-enhanced photothermal assistance are improved by 6.5 and 2.1 times, respectively. Our work offers a novel strategy for developing TPP-integrated fiber-optic tips, refines the theoretical framework of photothermal-assisted detection systems, and provides clear experimental evidence.

**Keywords:** fiber-optic hydrogen sensor; Tamm plasmon polariton; photothermal synergistic effect; dynamic response enhancement; cost-effective production

Wei XR, Liang YZ, Zhang XH et al. Multi-resonance enhanced photothermal synergistic fiber-optic Tamm plasmon polariton tip for high-sensitivity and rapid hydrogen detection. *Opto-Electron Sci* **4**, 240029 (2025).

## Introduction

Hydrogen ($H_2$), as a green renewable energy source, is anticipated to replace traditional fossil fuels in industries, construction, transportation, and other fields due to its excellent combustion performance and environmentally friendly characteristics[1,2]. However, $H_2$ is a highly

[1]School of Physics, Dalian University of Technology, Dalian 116024, China; [2]Liaoning Key Laboratory of Marine Sensing and Intelligent Detection, Dalian Maritime University, Dalian 116026, China; [3]Information Science and Technology College, Dalian Maritime University, Dalian 116026, China; [4]National Laboratory of Solid-State Microstructures, College of Engineering and Applied Sciences and Collaborative Innovation Center of Advanced Microstructures, Nanjing University, Nanjing 210093, China; [5]Key Laboratory of Intelligent Optical Sensing and Manipulation, Ministry of Education, Nanjing University, Nanjing 210093, China.

*Correspondence: YZ Liang, E-mail: yzliang@dlut.edu.cn; T Xu, E-mail: xuting@nju.edu.cn

Received: 11 November 2024; Accepted: 15 January 2025; Published online: 21 May 2025

flammable and explosive gas, with a risk of explosion when its concentration in the air exceeds 4%. Additionally, $H_2$ is colorless and odorless, difficult to perceive directly. Therefore, it is extremely crucial to develop high-performance $H_2$ sensors for real-time detection of $H_2$ concentration in these processes involving its production, storage, transportation, and utilization[3]. Optical sensors based on hydrogen-sensitive materials like palladium (Pd), platinum (Pt), and their alloys, have become prominent and feasible solutions for real-time detection[4–8]. Unlike traditional electrical sensors[9,10], these optical sensors exhibit a reduced risk of explosion and lower power consumption, making them more competitive for various application scenarios. Moreover, with the rapid development of Internet of Things (IoT) technology, optical sensors are increasingly focused on miniaturization and integration.

Fiber optic sensors, as integrated and miniaturized alternatives to prism or on-chip devices, combine optical sensing with optical transmission capabilities. They offer enhanced flexibility, robust resistance to electromagnetic interference, and the potential for remote monitoring and distributed measurement[11–18]. Consequently, considerable efforts have been devoted to developing highly sensitive and fast-response fiber-optic $H_2$ sensors using various resonance coupling mechanisms, such as Fabry-Perot (FP) interferometers[19,20], fiber Bragg gratings[21,22], tilted fiber Bragg gratings[23], Mach-Zehnder interferometers[24], fiber optic surface plasmon resonance[25,26], and the like. The response time of these fiber-optic sensors typically depends on the $H_2$ permeability of the $H_2$-sensitive material, which is negatively correlated with its thickness and positively correlated with the working temperature[27]. Therefore, increasing the operating temperature is an effective strategy to improve the response time of the $H_2$ sensor with fixed structural dimensions. Contemporarily, photothermal effects have been integrated into various emerging optoelectronic devices for their precise and non-contact heating capabilities[28–33]. This approach provides an all-optical pathway to develop temperature-assisted fiber-optic sensors for rapid $H_2$ detection[34,35]. Nevertheless, the theoretical analysis and experimental investigation of the photothermal effect in the reported photothermal-assisted $H_2$ detection remain insufficient, hindering the optimal utilization of the photothermal effect in these systems.

Despite significant advancements in developing high-performance fiber-optic $H_2$ sensors have been achieved, these efforts often rely on complex fabrication processes such as photolithography, fiber modification, and structural transfer, which restricts the potential for achieving low-cost and large-scale production of fiber-optic $H_2$ sensors. Tamm plasmon polariton (TPP), as a boundary state mode, is excited at the interface between the distributed Bragg reflector (DBR) and metal film[36–39]. The geometry structure supporting the TPP mode is constructed using only planar multilayer films, bypassing the requirement for photolithography or structural transfer methods. Consequently, TPP in multilayer films has attracted considerable attention in various fields, including biochemical sensing[40,41], filtering and absorption[42,43], nonlinear optics[44], and electro-optic modulation[45]. However, electric fields in TPP-based optical sensors are mainly concentrated inside the structure, resulting in relatively low sensitivity and thus not appropriate for bioassays. One effective solution is to replace the metal film with sensitive materials to achieve high-sensitivity detection of specific analytes[40], which is consistent with the principle of $H_2$ detection[46]. Furthermore, the excitation of TPP does not necessitate strict control of the angle and polarization of incident light. Therefore, it can be directly integrated into the fiber end facet without requiring special fiber treatment. Nevertheless, to the best of our knowledge, TPP-integrated fiber-optic devices constructed by multilayer planar films, including sensors and other optoelectronic devices, have not been experimentally reported until now.

In this paper, we experimentally integrate multilayer planar DBR and $H_2$-sensitive metal Pd onto the end facet of fiber for the first time, supporting the excitation of TPP and FP modes. By assigning distinct functions to different resonance modes, a multi-resonance enhanced photothermal synergistic FOTPP $H_2$ sensing tip is both theoretically and experimentally demonstrated. In this system, TPP mode with higher sensitivity is utilized for $H_2$ detection, while the high-absorption FP resonance enhances the photothermal catalytic effect, thereby improving the dynamic response speed of $H_2$ detection. We elucidate theoretically the $H_2$ sensing mechanism of TPP by comparing it with FP resonance, providing a novel design scheme for multilayer planar sensors. Furthermore, the dependence of TPP's sensitivity on Pd film thickness has also been thoroughly analyzed and discussed theoretically and experimentally. Due to the improved reproducibility demonstrated by the FOTPP tip with a thicker Pd film, we highlight its sensing perfor-

mance, including sensitivity, repeatability, and stability. Compared to traditional FP resonance sensing structures, the FOTPP $H_2$ sensing tip exhibits excellent $H_2$ detection performance and minimal cross-sensitivity due to its independence from Pd film deformation. Additionally, we provide a comprehensive theoretical and experimental investigation of the high-efficiency heating and catalytic effects of FP resonance photothermal effect, including their dependencies on resonance wavelength, laser power, and Pd film thickness. The results indicate that the FP resonance-enhanced photothermal effect significantly accelerates the response and recovery speeds of the FOTPP sensing tip and surpasses the photothermal assistance provided by non-resonance modes. This provides the necessary theoretical and experimental validation for the photothermal-assisted detection system.

## Structural design and analysis of sensing mechanism

Figure 1(a) and 1(b) depict three-dimensional schematic diagram and cross-section of the proposed FOTPP sensing tip, which consists of both dielectric DBR and $H_2$-sensitive metal Pd. The DBR is composed of 5 pairs of alternately stacked $Al_2O_3$ and $TiO_2$ dielectric layers, designed to create photonic bandgaps. The thicknesses of the $TiO_2$ and $Al_2O_3$ layers satisfy the Bragg condition: $n_i h_i = \lambda_{Bragg}/4$ ($i$ = 2, 3), where $n_i$ and $h_i$ represent the refractive index and thickness of $TiO_2$ and $Al_2O_3$, respectively, and $\lambda_{Bragg}$ represents the Bragg wavelength. In this design, the values of $n_2$ and $n_3$ are measured by the ellipsometer (M-2000 V), while the complex refractive indices of Pd and $PdH_x$ are taken from the reported literature[47], as shown in Supplementary information Fig. S1. Besides, $\lambda_{Bragg}$ is fixed at 400 nm with a 42 nm thick $TiO_2$ layer and a 60 nm thick $Al_2O_3$ layer, and the thickness of the top Pd film is denoted as $h_1$. The preparation of FOTPP tips is detailed in the "Sample preparation" section. The cross-sectional scanning electron microscope (SEM) image on the right side of Fig. 1(b) demonstrates the uniformity of periodically stacked layers. Additionally, the metallic Pd not only excites TPP at the Pd/DBR interface but also serves as an $H_2$ sensing layer. As shown in Fig. 1(c), there are both TPP and FP resonance modes generated in the FOTPP tip. The hydrogenation of the Pd film causes a redshift in the TPP resonance wavelength, thereby enabling $H_2$ detection through wavelength demodulation. Due to the inherent response recovery characteristics of Pd film, the FOTPP sensing tip also exhibits good repeatability. Furthermore, the photothermal effect induced by the FP resonance mode is employed to improve the response recovery speed of the FOTPP sensing tip.

Optical properties of the FOTPP tip are calculated by both the transfer matrix method (TMM) and the finite-difference time-domain (FDTD) method. Figure 2(a) shows the TMM-calculated dependence of reflection spectra on the thickness of Pd film. When there is no Pd film on the FOTPP tip, its reflection spectrum exhibits a

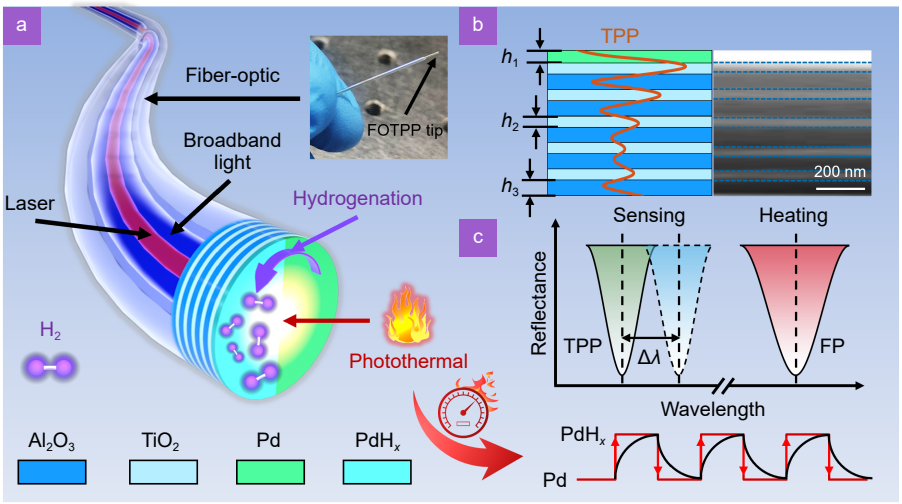


**Fig. 1 |** Photothermal synergistic TPP $H_2$ detection system integrated on the fiber tip. (**a**) Three-dimensional schematic of the fabricated fiber-optic TPP (FOTPP) tip with broadband halogen source (blue beam) and narrowband laser (red beam), along with a photograph of the actual fabricated FOTPP tip. (**b**) Its cross-section and SEM image for the FOTPP tip, where $h_1$, $h_2$, and $h_3$ denote the thicknesses of Pd, $TiO_2$, and $Al_2O_3$ layers, respectively. (**c**) Schematic of spectral working principle of photothermal synergistic FOTPP $H_2$ sensing tip and the response/recovery characteristics of resonance wavelength under photothermal (red curve) and non-photothermal (black curve) synergistic conditions.

primary bandgap around 400 nm. With the increased thickness of the Pd film, a resonance dip (labeled as $D_1$) appears within this bandgap, along with two resonance dips at longer wavelengths labeled as $D_2$ and $D_3$. The resonance depth of dip $D_1$ increases with the thickness of the Pd film, reaching a maximum near 50 nm. Besides, the effects of other structural parameters on the characteristic spectra are detailed in Supplementary information Fig. S2. For a direct comparison, the DBR is equivalent to a dielectric layer with an average RI of $\bar{n} = (n_2h_2 + n_3h_3)/(h_2 + h_3)$[48], serving as an FP resonance structure. Unlike the TPP resonance structure, the reflection spectra of the FP resonance structure exhibit four distinct orders of FP resonance dips, labeled as $D_1$', $D_2$', $D_3$', and $D_4$', as illustrated in Fig. 2(b). We further compared the $H_2$ detection sensitivity of the two different structures using TMM to demonstrate the superiority of the multilayer TPP resonance structure. Figure 2(c) illustrates the wavelength shift of the resonance dips of TPP (top panel) and FP (bottom panel) resonance structures after the hydrogenation of Pd films with different thicknesses. The results indicate that resonance dip $D_1$ exhibits higher sensitivity compared to dips $D_2$ and $D_3$. Furthermore, the sensitivity of the resonance dip $D_1$ decreases rapidly as the Pd film thickness increases before stabilizing. Therefore, considering potential processing errors, it is crucial to use a sufficiently thick Pd film to ensure high reproducibility in the sensitivity of FOTPP tips. Furthermore, the sensitivity of the FP resonance structure is comparable to that of $D_2$ and $D_3$, but less than half of the resonance dip $D_1$ mode in the FOTPP resonance structure for different thicknesses of Pd film. Therefore, the proposed FOTPP resonance structure demonstrates superior performance compared to the FP resonance structure for $H_2$ detection. The generation mechanisms of the resonance dips $D_1$, $D_2$, and $D_3$ are investigated through simulated electric field distribution. As shown in Fig. 2(d–f), resonance dip $D_1$ exhibits the strongest electric field at the DBR/Pd interface, gradually decaying within the DBR with a periodically modulated

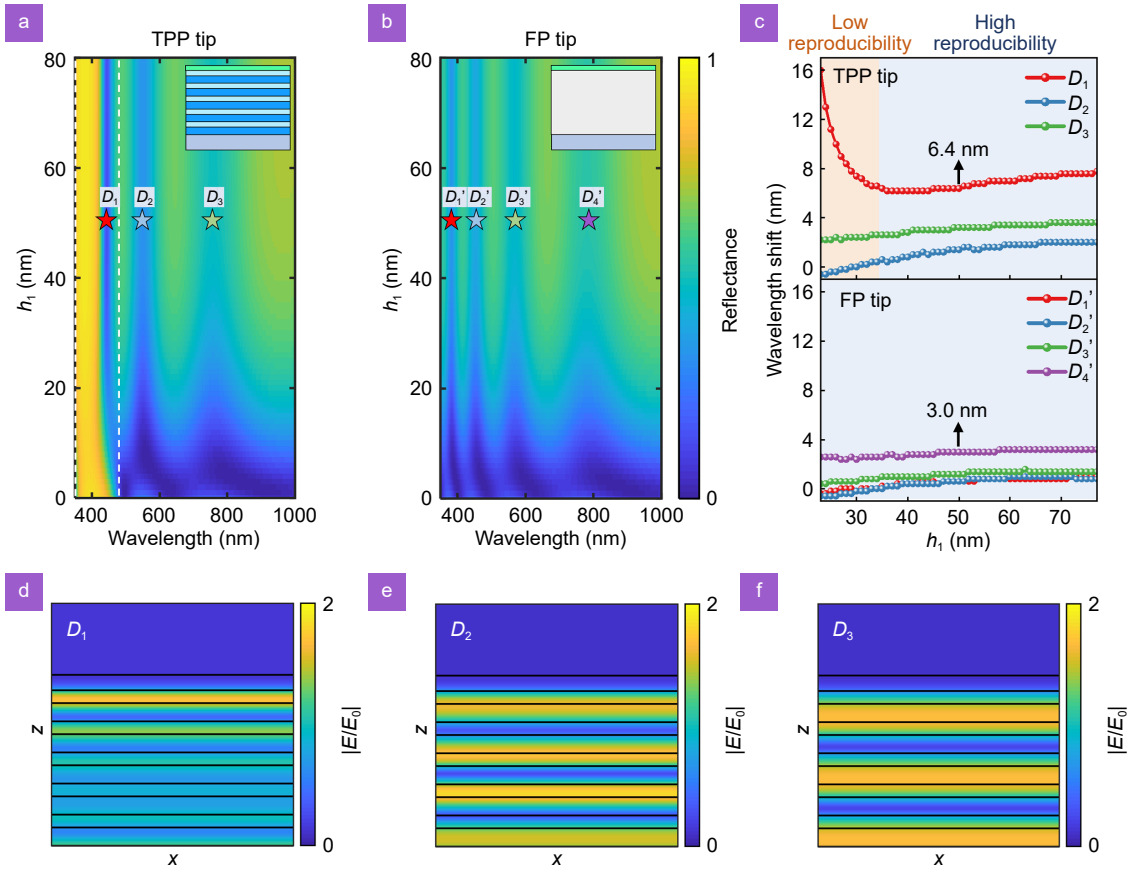


**Fig. 2 |** Photoelectric characteristics of the FOTPP tip for $H_2$ detection. TMM calculated the reflection spectra of (**a**) FOTPP and (**b**) FP tips with different thicknesses of Pd film. The white dashed line marks the main bandgap location of the DBR. (**c**) Wavelength shifts of the resonance dips of TPP (top panel) and FP (bottom panel) tips after hydrogenation at various thicknesses of Pd film. (**d–f**) Simulated electric field profiles for three resonance dips supported by the FOTPP tip with a 50 nm thick Pd film, where $E_0$ denotes the incident electric field intensity.

exponential envelope, a typical characteristic of TPP. In contrast, resonance dips $D_2$ and $D_3$ produce interference fringes with highly uniform intensity, indicating their origin from different orders of FP resonance. Consequently, the sensitivity of the TPP mode surpasses that of the FP resonance mode.

To explain this phenomenon, the response mechanism of TPP to the hydrogenation of the Pd film is explored theoretically. Figure 3(a) depicts the electric field distribution curves of TPP before and after hydrogenation for a 50 nm thick Pd film. These results indicate that, after Pd hydrogenation, the electric field intensity of the TPP weakens, accompanied by a decrease in the penetration depth of the TPP into the DBR ($L_{\mathrm{Bragg}}$). Here, the penetration depth is defined as the minimum of the electric field envelope. Additionally, Fig. 3(b, c) illustrates the dependence of the TPP electric field on the thickness of Pd film before and after hydrogenation, while Fig. 3(d) summarizes the maximum electric field intensity of TPP at the Pd/DBR interface. Both $L_{\mathrm{Bragg}}$ and the electric field intensity of TPP mode increase with the thickness of the Pd/PdH$_x$ layer, meanwhile they tend to stabilize as the thickness of Pd/PdH$_x$ approaches 50 nm, indicating a correlation with reflection intensity. Additionally, both $L_{\mathrm{Bragg}}$ and the electric field intensity of TPP before hydrogenation are always greater than those after hydrogenation, which is attributed to the reduced reflection intensity of Pd film after hydrogenation, as shown in Fig. 3(e). Therefore, $L_{\mathrm{Bragg}}$ is positively correlated with the reflection intensity of the metal film on top of the DBR because greater reflection intensity excites stronger TPP resonance, in turn requiring a longer $L_{\mathrm{Bragg}}$ for attenuation. This phenomenon is key to achieving the $H_2$-induced wavelength shift of the TPP resonance. We further elucidate the response mechanism of TPP mode through its phase-matching condition as below[49]:

$$2\bar{n}L_{\mathrm{Bragg}} \cdot \frac{\omega - \omega_{\mathrm{Bragg}}}{c} = \varphi_{\mathrm{Pd/PdH}_x}\,, \tag{1}$$

where $\omega$ and $\omega_{\mathrm{Bragg}}$ is the resonance angular frequency of TPP and Bragg frequency, $c$ is the speed of light, and

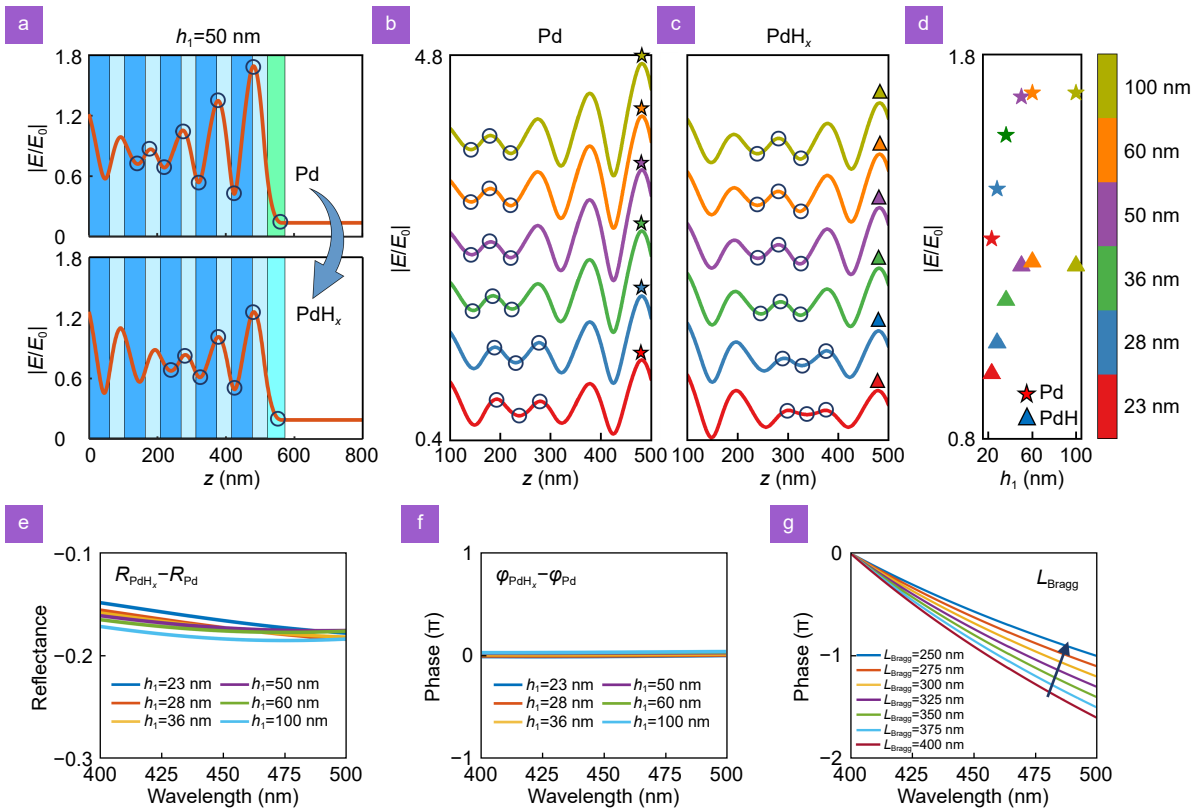


**Fig. 3 |** Response mechanisms of resonance wavelength in TPP mode. (**a**) Calculated electric field distribution at the resonance wavelength of TPP supported by the FOTPP tip before (top panel) and after hydrogenation (bottom panel). The dependence of the electric field distribution of TPP (**b**) before and (**c**) after hydrogenation on the thickness of the Pd film. The individual electric field curves are shifted upwards for clarity. The circle marks indicate the position range of $L_{\mathrm{Bragg}}$ (near the minimum of the electric field envelope). (**d**) The maximum electric field intensity of TPP at the Pd/DBR interface as a function of Pd film thickness. (**e**) Reflection intensity difference and (**f**) reflection phase difference between PdH$_x$ and Pd films at different thicknesses. (**g**) Dependency of the total phase contribution of the DBR on the penetration depth of TPP in DBR ($L_{\mathrm{Bragg}}$).

$\varphi_{Pd/PdHx}$ is the reflection phase of Pd/$PdH_x$. The left and right sides of the equation represent the total phase contributions of the DBR and the Pd/$PdH_x$ film to TPP resonance. In contrast, the phase matching condition for FP resonance is also presented as:

$$2\bar{n}h \cdot \frac{\omega'}{c} + \varphi_{Pd/PdH_x} = 2\pi N\,, \tag{2}$$

where $\omega$' is the angular frequency of FP resonance mode, $h$ is the total thickness of DBR, and $N$ is an integer. Because the above two equations for both resonance modes incorporate the total phase contribution of the metal film, the reflection phases of the Pd and $PdH_x$ films are calculated and shown in Fig. S3. Figure 3(f) illustrates the reflection phase difference ($\varphi_{PdHx} - \varphi_{Pd}$) before and after the hydrogenation of the Pd film. The results show that the change in the reflection phase of Pd films with different thicknesses before and after hydrogenation is minor. According to Eq. (2), the variation of the frequency of the FP resonance mode depends mainly on the difference between $\varphi_{PdHx}$ and $\varphi_{Pd}$ (other terms are constant or have negligible variation). Therefore, the wavelength shift of the FP resonance mode is relatively small. Different from the FP resonance mode, the wavelength shift of the TPP resonance mode mainly originates from the variation of $L_{Bragg}$. As depicted in Fig. 3(g), the $L_{Bragg}$ variation significantly affects the total phase contribution of the DBR, resulting in a significant resonance wavelength shift of the TPP. Differentiating Eq. (1) with respect to $L_{Bragg}$, we have:

$$\frac{\mathrm{d}\omega}{\mathrm{d}L_{Bragg}} = \frac{c}{2\bar{n}L_{Bragg}}\left(-\frac{\varphi_{Pd/PdH_x}}{L_{Bragg}} + \frac{\mathrm{d}\varphi_{Pd/PdH_x}}{\mathrm{d}L_{Bragg}}\right), \tag{3}$$

where $\mathrm{d}\varphi_{Pd/PdHx}/\mathrm{d}L_{Bragg}$ approaches to 0 ($\mathrm{d}\varphi_{Pd/PdHx}$ is minor) as well as both $\varphi_{Pd}$ and $\varphi_{PdHx}$ are always negative, this derivative is always greater than 0, that is, the resonance angular frequency of TPP is positively correlated with $L_{Bragg}$. Therefore, we demonstrate that the hydrogenation of the Pd film results in a reduction of $L_{Bragg}$, thus causing the redshift of TPP resonance wavelength. Moreover, the second-order differential of Eq. (1) is approximated as follows:

$$\begin{aligned}\frac{\mathrm{d}^2\omega}{\mathrm{d}L_{Bragg}^{\ 2}} &= \frac{c}{2\bar{n}L_{Bragg}} \\ &\left(\frac{\mathrm{d}^2\varphi_{Pd/PdH_x}}{\mathrm{d}L_{Bragg}^{\ 2}} - \frac{2\mathrm{d}\varphi_{Pd/PdH_x}}{L_{Bragg}\mathrm{d}L_{Bragg}} + \frac{2\varphi_{Pd/PdH_x}}{L_{Bragg}^{\ 2}}\right) \\ &\approx \frac{c\varphi_{Pd/PdH_x}}{\bar{n}} \cdot \frac{1}{L_{Bragg}^{\ 3}}\end{aligned}. \tag{4}$$

Since Eq. (4) is always less than 0, the resonance frequency of TPP exhibits a greater variation rate when $L_{Bragg}$ is smaller. As previously mentioned, $L_{Bragg}$ is positively correlated with Pd film's thickness. This indicates that the sensitivity of TPP is negatively correlated with the thickness of the Pd layer when the Pd thickness is relatively small, which is consistent with the result of Fig. 2(c). However, in this case, $L_{Bragg}$ has a strong dependence on the Pd film's thickness, resulting in poor robustness of the FOTPP tip's sensitivity. The strong dependence of sensitivity on the thickness of the $H_2$-sensitive material is also a common issue for many $H_2$ sensors. To address this issue, the thickness of the Pd film is increased to 50 nm in the experiment to minimize the dependence of $L_{Bragg}$ on Pd film thickness, ensuring that the fabricated FOTPP tip has relatively stable sensitivity within the permissible error range. Furthermore, as shown in Fig. 2(c), the FOTPP tip exhibits more than twice the sensitivity compared to the FP resonance structure, even for the thicker Pd film. Therefore, the FOTPP tip with a thicker Pd film simultaneously offers the advantages of high sensitivity and high reproducibility in fabrication.

## Hydrogen sensing application of photothermal synergistic FOTPP tip

The fabricated FOTPP tip is employed in $H_2$ detection to experimentally validate the rationalization of the proposed theory. Figure 4(a) illustrates the schematic diagram of the detection setup. Different $H_2$ concentrations are prepared using the mixture of high-purity nitrogen and high-purity $H_2$ in various proportions in a gas chamber controlled by two mass flow meters. The FOTPP sensing tip is placed inside the gas chamber, and a terminal reflection spectroscopy system captures the spectra and dynamically collects the resonance wavelength of TPP. As shown in Fig. 4(b), the experimentally measured reflection spectra of the FOTPP tip (top panel), without a Pd film and with a 50 nm thick Pd film, exhibit spectral characteristics consistent with theoretical alculations (bottom panel). This indicates that the designed FOTPP tip can support three distinct resonance modes simultaneously. The resonance intensity discrepancy of dip $D_1$ is mainly attributed to the differences in the permittivity of the metal Pd, as well as thickness deviation, roughness, and imperfect uniformity of multilayer film. The sensitivity of the FOTPP tip is further assessed by placing it in different $H_2$ concentrations. Figure 4(c)

illustrates the experimental spectra of the FOTPP tip at varying $H_2$ concentrations, revealing a redshift of TPP with increasing $H_2$ concentration. To demonstrate the response recovery properties and signal-to-noise ratio of the FOTPP tips, the gas in the chamber is cyclically switched between 100% $N_2$ and a specific $H_2$ concentration, maintaining each time interval of 300 s. The $H_2$ concentration gradually increases from 0% to 3.5%, then decreases from 3.5% back to 0%. This detection concentration range enables real-time quantitative monitoring of $H_2$ concentration in applications such as $H_2$ production and storage facilities, fuel cell systems, and the chemical industry, thereby addressing the safety requirements in industrial and energy storage and other fields[3]. Besides, according to our laboratory's safety management regulations, the case of $H_2$ concentration excessing 4% is not considered. Figure 4(d) and 4(e) show the amount of wavelength redshifts and real-time wavelength response of the FOTPP tip during the process. Experimental results indicate that the resonance wavelength of TPP is approximately linearly correlated with the $H_2$ concentration, with the sensitivity $S$ for both cycles remaining nearly consistent at approximately 0.661 nm/1%. The discrepancy between experimental and theoretical sensitivities is attributed to the incomplete hydrogenation of the Pd film and processing errors. In general, the limit of detection is defined as $3\sigma/S$, where $\sigma$ represents the standard deviation of the baseline (~0.0163 nm, as shown in Supplementary information Fig. S5(b)). Therefore, the ideal limit of detection of the sensor is determined to be 0.074%, showing the potential of FOTPP tips for detecting low $H_2$ concentrations. Additionally, after responding at different $H_2$ concentrations, the resonance wavelengths of TPP return to the initial positions in high-purity $N_2$, demonstrating good response recovery characteristics. Furthermore, we demonstrate that the resonance wavelength shift of TPP has a linear relationship with the external temperature, as shown in Fig. 4(f) and 4(g). Since the FOTPP $H_2$ sensor does not rely on the deformation of a suspended thin film, it exhibits a

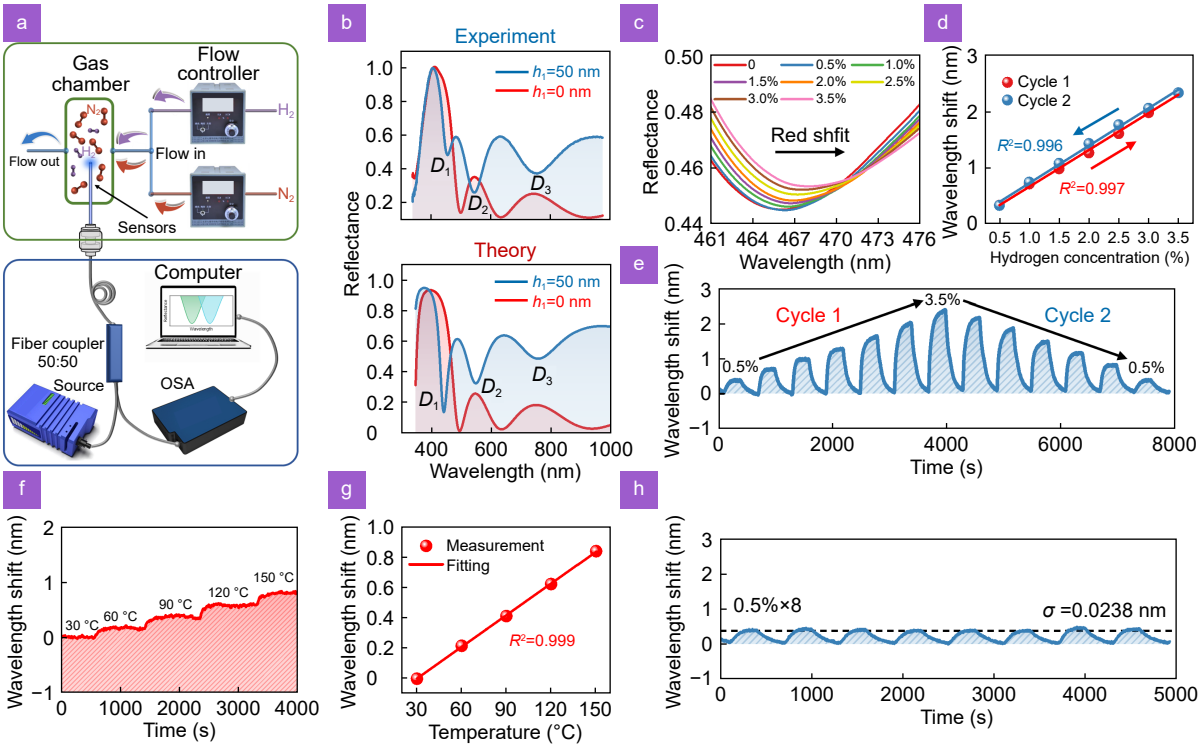


**Fig. 4 |** Experimental measurements of $H_2$ concentration using the fabricated FOTPP tip. (**a**) Schematic of the experimental setup for $H_2$ detection, highlighting the gas sensing and spectral analysis systems in the green and blue boxes, respectively. (**b**) Experimentally measured (top panel) and theoretically calculated (bottom panel) reflection spectra of the FOTPP tip without a Pd film and with a 50 nm thick Pd film. (**c**) Reflection spectra of the FOTPP tip under various $H_2$ concentrations ranging from 0.5% to 3.5%. (**d**) Wavelength redshifts and (**e**) real-time response of wavelength shift for the FOTPP tip at both increasing and decreasing $H_2$ concentration pulses, ranging from 0.5% to 3.5% and 3.5% to 0.5%. (**f**) Real-time wavelength shift response of TPP supported by the FOTPP tip under different working temperatures. (**g**) The relationship between the amount of wavelength shifts of TPP and working temperatures. (**h**) The wavelength response of the FOTPP tip in continuously repeated 0.5% $H_2$ concentration. The black dashed line represents the locations of the average wavelength shifts.

low temperature sensitivity of just 0.0072 nm/°C. This indicates that the FOTPP tip possesses relatively small cross-sensitivity, thereby enhancing its suitability for practical environmental monitoring applications. Furthermore, the FOTPP tip undergoes 8 cycles of response and recovery pulses in a 0.5% $H_2$ concentration to demonstrate its repeatability, as depicted in Fig. 4(h). The average response of the FOTPP tip in multiple detections of the 0.5% $H_2$ concentration has a wavelength shift of 0.365 nm with a standard deviation of 0.0238 nm. The small standard deviation confirms the FOTPP tip' capability for repeated detection of low concentrations of $H_2$ and its long-term durability. In addition to the FOTPP tip with a 50 nm thick Pd film, the sensing performance of FOTPP tips with 28 nm and 36 nm Pd films is also shown in Fig. S4. Experimentally, the trend in sensitivity variation, as illustrated in Fig. S4(c), is consistent with the theoretical calculations in Fig. 2(c). Moreover, to demonstrate the advantages of the FOTPP tip, the quantitative comparison of sensing performances between our work and other recent works is listed in Table S1. The comparison results indicate that the proposed FOTPP tip exhibits excellent sensing performance without the need for complex fabrication processes.

In addition to $H_2$ detection sensitivity, the dynamic response speed of the sensor is also an important factor in early warning applications for $H_2$ leakage. According to the Arrhenius equation[50], the rate of the H-Pd reaction is positively correlated with temperature. Therefore, increasing the surface temperature of the $H_2$ sensors is an effective method to improve its response time. Building on the multi-resonance characteristics of FOTPP tips, we further employ the FP resonance mode within the same structure to enhance light absorption, enabling a localized and efficient photothermal effect at the fiber tip while ensuring no crosstalk between photothermal assistance and $H_2$ sensing. Before further discussing the sensing performance of the photothermal-assisted FOTPP sensing tip, we will first provide a detailed demonstration of the photothermal effect in the FOTPP structure. Figure 5(a) illustrates the simulated absorption spectrum of the FOTPP tip before and after hydrogenation. There are three distinct absorption peaks corresponding to TPP and two different orders of FP resonance modes. As a representative example, a 785 nm laser (MDL-E-785-30 mW) located at the absorption peak is employed, while a 980 nm laser (LSR980H-4W-FC) situated at the absorption dip is used for comparison. The reasons for selecting a broad absorption peak rather than a narrow absorption peak (~550 nm) for photothermal-assisted effects are summarized as two aspects: (1) a broad absorption peak exhibits excellent tolerance to deviation between the laser wavelength and the absorption peak; (2) the photothermal effect enhanced by a broad absorption peak demonstrates greater stability and reduced temperature cross-sensitivity when the ambient environment changes. The loaded power of these two lasers measured using the optical power meter (S130VC) is 7 mW, as shown in Fig. S5(a). Figure 5(b) illustrates the effect of introducing these two lasers on the resonance wavelength of TPP. Due to the change in the permittivity of the materials induced by the generated photothermal effect, the TPP resonance wavelength undergoes a redshift. Specifically, the redshift induced by the 785 nm laser is larger, indicating a higher generating temperature. Moreover, we demonstrate that the FOTPP tip exhibits excellent stability when exposed to air for a prolonged duration, either under laser illumination or non-laser illumination (as shown in Fig. S5(b–d)). To quantitatively describe the temperatures generated by these two lasers, comprehensive photothermal numerical calculations are performed. The scaled absorbed power $Q_{\rm abs}$ can be expressed by the following equation[51]:

$$Q_{\rm abs} = \frac{\varepsilon_0 \omega \varepsilon'' |E|^2}{\int {\rm Re}\,(P_{\rm inc}) \cdot {\rm d}S_{\rm sim}} \cdot I_{\rm Laser} \cdot S_{\rm sim}\ , \tag{5}$$

where $\varepsilon_0$ and $\varepsilon''$ represent the vacuum permittivity and the imaginary part of the permittivity of the materials, respectively. $E$ is the electric field intensity in the materials. $P_{\rm inc}$ and $S_{\rm sim}$ are the Poynting vectors and the illuminated area (simulated region) of the incident light, respectively. $I_{\rm Laser}$ is the power density of the laser, defined as the ratio of laser power to spot area. Since the spot diameter is equal to the fiber core diameter (400 μm), $I_{\rm Laser}$ is determined to be $5.573\times10^4$ W/m$^2$. Based on Eq. (5), the scaled absorption power distributions of the FOTPP tip at wavelengths of 785 nm and 980 nm are calculated and illustrated in Fig. 5(c) and 5(d). The absorbed power is concentrated within the Pd film, with the FOTPP tip showing greater absorbed power for the 785 nm laser compared to the 980 nm laser. This indicates that resonance modes can more effectively absorb light energy, thereby enhancing light-to-heat energy conversion. According to the distribution of absorption power, the thermodynamic properties of the FOTPP resonance structure are further performed using the finite element

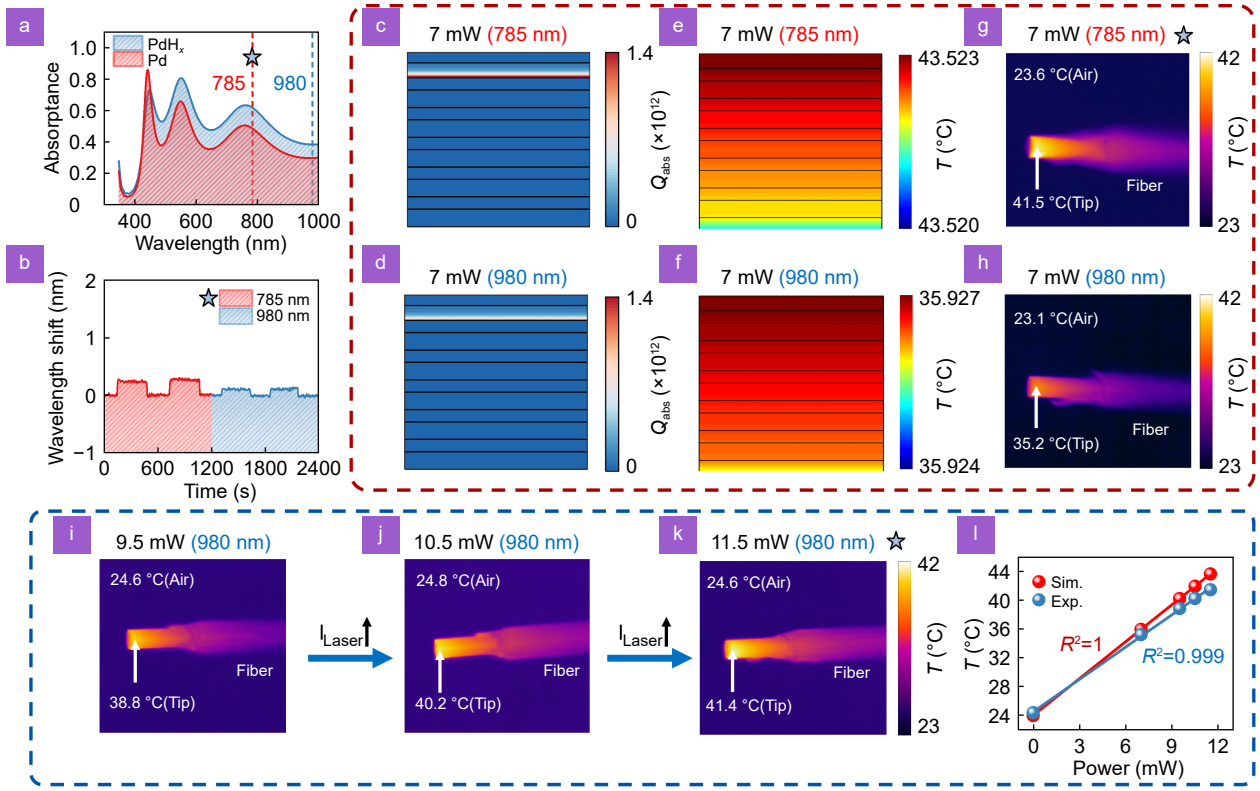


**Fig. 5 |** Theoretical and experimental characterization of photothermal effect in the FOTPP tip with a 50 nm thick Pd film. (**a**) Simulated absorption spectra of the FOTPP tip before and after hydrogenation. (**b**) The effect of two 7 mW lasers with different wavelengths on the resonance wavelength of TPP. Calculated absorbed power and temperature distributions at wavelengths of (**c**, **d**) 785 nm and (**e**, **f**) 980 nm. Experimentally measured thermal images of the FOTPP tip under (**g**) 785 nm and (**h**) 980 nm laser illumination. (**i**–**k**) Thermal images of the FOTPP tip illuminated with three higher-power 985 nm lasers (9.5 mW, 10.5 mW, and 11.5 mW). The peak temperature of the fiber-optic tip and the ambient temperature are indicated in the thermal images. (**l**) Simulated and measured peak temperature at the FOTPP tip under different laser powers. For clarity, scenarios illuminated by 7 mW and higher power lasers are differentiated by enclosing them in red and blue boxes, respectively.

method. Figure 5(e) and 5(f) illustrate the temperature distribution of the FOTPP structure under these two laser illuminations. The temperature within the multilayer structure is nearly uniform in steady state, with optical heating from the 785 nm laser and the 980 nm laser resulting in temperatures of approximately 43.5 °C and 35.9 °C, respectively. In the experiment, thermal images of the FOTPP tip illuminated with these two lasers (785 nm and 980 nm) are captured directly using a high-resolution infrared thermal camera (FOTRIC 220 s), as depicted in Fig. 5(g) and 5(h). The peak temperature at the fiber tip and the ambient temperature are also indicated in these figures. The experimental results are in near agreement with numerical simulations, thereby validating the relationship between the photothermal effect and the resonance wavelength. Additionally, Fig. 5(i–l) provide theoretical and experimental evidence that the photothermal effect is proportional to laser power. This result also shows that the laser with non-resonance wavelengths requires higher power to achieve the same photothermal effect. Therefore, the resonance absorption effect of the structure can effectively enhance and regulate the photothermal effect.

The photothermal-synergistic sensing setup for rapid $H_2$ detection is developed based on the aforementioned multi-resonance enhancement scheme. As depicted in Fig. 6(a), the laser and broadband halogen light source are simultaneously introduced into the FOTPP tip via fiber-optic jumpers. Additionally, a filter is placed in front of the spectrometer to cut off reflected light with wavelengths longer than 750 nm, preventing potential damage from reflected lasers. Noteworthy, all tests are conducted in a thermally stable environment, where the laser output power remains stable, leading to minimal temperature variations on the sensor surface. In view of the extremely small temperature sensitivity of TPP, the wavelength shift induced by slight temperature variations is negligible, with only a corresponding adjustment

of the sensor's baseline at different operating temperatures. Figure 6(b) shows the real-time wavelength shift response of the TPP mode under photothermal assistance from both 785 nm (top panel) and 980 nm (bottom panel) lasers, which indicates that the FOTPP tip maintains excellent response and recovery characteristics and signal-to-noise ratio under photothermal assistance, as like as that under non-photothermal conditions. To demonstrate the advantages of photothermal-assisted $H_2$ detection, Fig. 6(c) demonstrates the response and recovery curve of TPP at a 3.5% $H_2$ concentration under both non-photothermal and photothermal conditions. Without the photothermal synergy, the response and recovery times of $H_2$ detection are 122 s and 179 s, respectively. However, with the photothermal assistance of a 785 nm laser, the response and recovery times are reduced by approximately 85% and 53% (~19 s and 85 s) and are shorter than those achieved with a 980 nm laser (~25 s and 104 s). These results demonstrate that the photothermal catalytic effect significantly improves the response and recovery speeds of the FOTPP tip, with the effect being more pronounced under resonance-enhanced photothermal conditions. Figure 6(d) and 6(e) summarize the response and recovery times of the FOTPP tip at various $H_2$ concentrations under three different conditions. The results at other $H_2$ concentrations further highlight the superiority of resonance-enhanced photothermal assistance in improving the dynamic response/recovery speed. Furthermore, the dynamic response and recovery speed of the photothermal-assisted FOTPP tip exhibits a positive correlation with $H_2$ concentration, as the adsorption and diffusion rates of $H_2$ molecules are faster at higher concentrations. The influence of the photothermal effect on the wavelength shift of the TPP is also thoroughly explored, as illustrated in Fig. 6(f). It is noteworthy that the photothermal effect reduces wavelength shifts of the TPP mode, particularly in high-concentration $H_2$ environments. This is because the increase in temperature causes the Pd lattice to expand, facilitating the diffusion of $H_2$ into the surrounding environment, thereby reducing the binding ratio of H and Pd. Despite this reduction in wavelength shift, the sensitivity remains sufficient for $H_2$ detection application. Moreover, recent research has indicated that an increase in temperature is beneficial for $H_2$ detection in high relative humidity environments[8]. Therefore, the photothermal effect can also provide an effective strategy for overcoming environmental interference such as high relative humidity, further highlighting the importance of developing photothermal synergistic detection

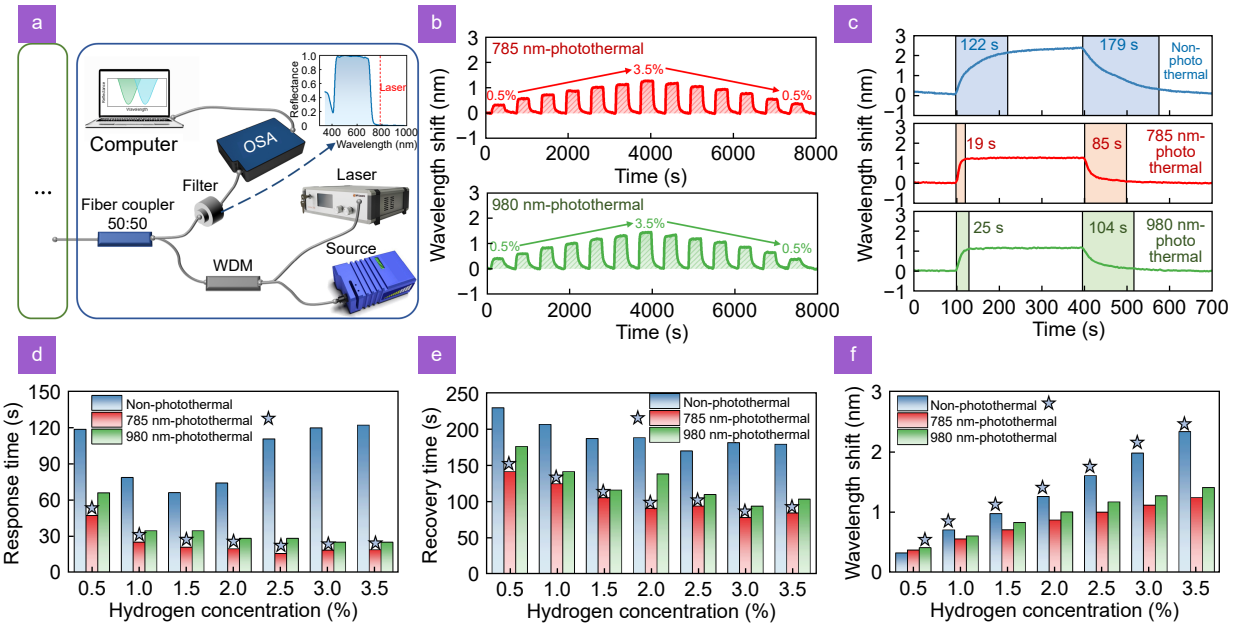


**Fig. 6 |** Quantitatively assessment of the sensing performance of resonance-enhanced photothermal synergistic FOTPP tip with a 50 nm thick Pd film. (**a**) Schematic of the optical setup used for photothermal assistance. (**b**) Real-time wavelengths shift of TPP mode supported by the FOTPP tip under 785 nm laser illumination (top panel) and 980 nm laser illumination (bottom panel). (**c**) Response recovery curve of TPP at a 3.5% $H_2$ concentration under non-photothermal (blue curve), 785 nm-photothermal (red curve), and 980 nm-photothermal (green curve) conditions. Comparison of (**d**) response time, (**e**) recovery time, and (**f**) wavelength redshifts for the FOTPP tip at various $H_2$ concentrations under three different photothermal conditions.

technology. Finally, we discuss the effect of Pd film's thickness on the photothermal synergistic $H_2$ detection system, as depicted in Fig. S6. This theoretical and experimental evidence provides valuable insights into optimizing the photothermal-assisted detection technology.

## Conclusions and discussion

In conclusion, we have successfully designed and fabricated a multi-resonance enhanced photothermal synergistic FOTPP $H_2$ sensing tip. Through numerical simulations and theoretical analysis, we have demonstrated that the TPP response to $H_2$ is primarily attributed to changes in phase-matching conditions, driven by the decreased penetration depth within the PC. This distinctive operational mechanism enhances the sensitivity of TPP to more than twice that of the FP resonance mode. Experimentally, the sensitivity of the FOTPP $H_2$ sensing tips surpasses many fiber-optic $H_2$ sensors relying on Pd film deformation, with extremely low temperature cross-sensitivity. Furthermore, the relationship between TPP sensitivity and Pd film thickness has been confirmed both theoretically and experimentally.

In addition to the TPP resonance mode, we also achieve an efficient photothermal effect through the FP resonance mode in the FOTPP structure, significantly catalyzing the reaction between Pd and H. Theoretical and experimental results demonstrate that FP resonance absorption effectively improves the optical heating induced by the photothermal effects, thereby further reducing the sensor's response and recovery times. In particular, the response and recovery speeds of the FOTPP sensor are improved by 6.5 times and 2.1 times, respectively, at an $H_2$ concentration of 3.5%. In terms of fabrication, the FOTPP sensing tip offers unparalleled advantages over traditional sensors, typically requiring lithography or structural transfer. It can be fabricated simply through thin film deposition, enabling cost-effective batch production of the sensor. Thus, our work not only paves a new path for integrated TPP devices but also offers crucial theoretical reinforcement and experimental verification for photothermal-assisted sensing technology.

Notably, in certain circumstances, molecules such as $H_2O$, CO, and $NO_x$ can strongly bind to the surface of $H_2$-sensitive materials, effectively inhibiting the adsorption and dissociation of $H_2$, which ultimately leads to sensor deactivation. Fortunately, previous studies have demonstrated that elevated temperatures can effectively mitigate this deactivation issue[8]. Therefore, although the present study only focuses on sensing applications under conventional environmental conditions, the precisely controllable photothermal synergistic detection technique provides a potential strategy to overcome the competitive adsorption of $H_2O$ and other molecules, thereby enhancing the environmental adaptability of hydrogen sensors.

## Materials and methods

**Numerical simulation approach:**

In the TMM calculation, the transfer matrix of each layer can be determined by the following forms:

$$M_i = \begin{pmatrix} \cos\delta_i & -\dfrac{\mathrm{i}}{\eta_i}\sin\delta_i \\ -\mathrm{i}\eta_i\sin\delta_i & \cos\delta_i \end{pmatrix}, \tag{6}$$

where $\delta_i$ and $\eta_i$ satisfy the following equation:

$$\delta_i = \frac{\omega}{c} n_i h_i, \quad \eta_i = \sqrt{\frac{\varepsilon_0}{\mu_0}} n_i \,. \tag{7}$$

Among them, $n_i$ and $h_i$ represent the refractive index and thickness of each layer. $\varepsilon_0$ and $\mu_0$ are vacuum permittivity and vacuum magnetic permeability. The transmission behavior of incident light in multilayer dielectrics is expressed as the multiplication of the transfer matrix of each dielectric layer:

$$\begin{aligned} \begin{pmatrix} E_1 \\ H_1 \end{pmatrix} &= \left(\prod_{i=1}^{\mathrm{N}} M_i\right) \begin{pmatrix} E_{\mathrm{N}+1} \\ H_{\mathrm{N}+1} \end{pmatrix} \\ &= \begin{pmatrix} A & B \\ C & D \end{pmatrix} \begin{pmatrix} E_{\mathrm{N}+1} \\ H_{\mathrm{N}+1} \end{pmatrix}, \end{aligned} \tag{8}$$

where A, B, C, D are the elements of the total matrix of 2×2. The reflection coefficient of the multilayer structure can be written as follows:

$$r = \frac{A\eta_0 + B\eta_0\eta_{\mathrm{N}+1} - C - D\eta_{\mathrm{N}+1}}{A\eta_0 + B\eta_0\eta_{\mathrm{N}+1} + C + D\eta_{\mathrm{N}+1}} \,. \tag{9}$$

In the FDTD simulation, a two-dimensional simulation is employed in the $x$–$z$ plane, with periodic boundary conditions and perfectly matched layers applied along the $x$ and $z$ directions. The incident light has an electric field amplitude of 1 V/m, with the incident and polarization directions along the $z$ and $x$ axes, respectively.

In the thermal simulation, the temperature of the ambient surroundings is fixed to 24 °C. We assume that the temperature returns to the ambient temperature after propagating 1 mm inside the fiber core. Besides, the top of the FOTPP tip is cooled convectively via natural convection with a convective heat transfer coefficient of 10 W/(m²·K). The material parameters used in the thermal simulations are summarized in Table 1.

**Table 1 |** Heat transfer properties of the materials in our thermal simulations.

| Materials | Density ($kg·m^{-3}$) | Specific heat ($J·(kg·K)^{-1}$) | Thermal conductivity ($W·(m·K)^{-1}$) |
|---|---|---|---|
| Pd | 12023 | 240 | 72 |
| $TiO_2$ | 4950 | 690 | 7.4 |
| $Al_2O_3$ | 3900 | 796 | 28 |
| $SiO_2$ | 2203 | 709 | 1.38 |

**Table 2 |** The coating process parameters of the atomic layer deposition technique.

| Thin film | Precursors | Pulse (ms) | Purge (s) | Precursor temperature (°C) | Deposition temperature (°C) | Cycle number |
|---|---|---|---|---|---|---|
| $Al_2O_3$ | Trimethylaluminum | 20 | 20 | Room temperature | 150 | 580 |
| | Water | 20 | 25 | Room temperature | | |
| $TiO_2$ | Titanium tetrakis(dimethylamide) | 100 | 20 | 70 | 150 | 715 |
| | Water | 20 | 25 | Room temperature | | |

**Material:**

The multimode optical fiber for sensing is purchased from Changfei Optical Fiber & Cable Co., Ltd, with core/cladding/coating diameters of 400/430/730 μm and a numerical aperture (NA) of 0.37. The materials of the core, cladding, and coating are high-purity quartz, fluorine-containing acrylic resin, and Ethylene-tetrafluoroethylene, respectively, and the optical fiber cutter was purchased from OSCOM Technology Co., Ltd.

**Sample Preparation:**

Initially, commercial fiber optics are cut using an optical fiber cutter to achieve a clean and flat fiber end facet. Subsequently, 5 pairs of $Al_2O_3$ and $TiO_2$ thin films are sequentially deposited on the fiber end facet using the atomic layer deposition (MNT-S100Oz-L3S1) technique with a vacuum degree of 20 Pa. The specific coating process parameters are shown in Table 2. Finally, a single layer of Pd film is deposited on top of the DBR using magnetron sputtering (Quorum Q300T+) with the sputtering current of 40 mA for a time of 100 s.

## References


1. Ould Amrouche S, Rekioua D, Rekioua T et al. Overview of energy storage in renewable energy systems. *Int J Hydrogen Energy* **41**, 20914–20927 (2016).
2. Yue ML, Lambert H, Pahon E et al. Hydrogen energy systems: a critical review of technologies, applications, trends and challenges. *Renew Sustain Energy Rev* **146**, 111180 (2021).
3. Sripriya, Meda US. Market study of hydrogen sensors and sensing systems. *ECS Trans* **107**, 4489–4502 (2022).
4. Tittl A, Mai P, Taubert R et al. Palladium-based plasmonic perfect absorber in the visible wavelength range and its application to hydrogen sensing. *Nano Lett* **11**, 4366–4369 (2011).
5. Baldi A, Narayan TC, Koh AL et al. *In situ* detection of hydrogen-induced phase transitions in individual palladium nanocrystals. *Nat Mater* **13**, 1143–1148 (2014).
6. Matuschek M, Singh DP, Jeong HH et al. Chiral plasmonic hydrogen sensors. *Small* **14**, 1702990 (2018).
7. Wen L, Sun ZW, Zheng QL et al. On-chip ultrasensitive and rapid hydrogen sensing based on plasmon-induced hot electron–molecule interaction. *Light Sci Appl* **12**, 76 (2023).
8. Tomeček D, Moberg HK, Nilsson S et al. Neural network enabled nanoplasmonic hydrogen sensors with 100 ppm limit of detection in humid air. *Nat Commun* **15**, 1208 (2024).
9. Korotcenkov G, Han SD, Stetter JR. Review of electrochemical hydrogen sensors. *Chem Rev* **109**, 1402–1433 (2009).
10. Liu Q, Yao JY, Wang YP et al. Temperature dependent response/recovery characteristics of Pd/Ni thin film based hydrogen sensor. *Sens Actuators B Chem* **290**, 544–550 (2019).
11. Caucheteur C, Guo T, Albert J. Review of plasmonic fiber optic biochemical sensors: improving the limit of detection. *Anal Bioanal Chem* **407**, 3883–3897 (2015).
12. Jing JY, Liu K, Jiang JF et al. Highly sensitive and stable probe refractometer based on configurable plasmonic resonance with nano-modified fiber core. *Opto-Electron Adv* **6**, 220072 (2023).
13. Wang Q, Wang L. Lab-on-fiber: plasmonic nano-arrays for sensing. *Nanoscale* **12**, 7485–7499 (2020).
14. Xiong YF, Xu F. Multifunctional integration on optical fiber tips: challenges and opportunities. *Adv Photonics* **2**, 064001 (2020).
15. Zhao Y, Tong RJ, Xia F et al. Current status of optical fiber biosensor based on surface plasmon resonance. *Biosens Bioelectron* **142**, 111505 (2019).
16. Liu HH, Hu DJJ, Sun QZ, Wei L, Li KW et al. Specialty optical fibers for advanced sensing applications. *Opto-Electron Sci* **2**, 220025 (2023).
17. Jiang BQ, Hou YG, Wu JX, Ma YX, Gan XT et al. In-fiber photoelectric device based on graphene-coated tilted fiber grating. *Opto-Electron Sci* **2**, 230012 (2023).
18. Yin SY, Guo Q, Liu SR et al. Three-dimensional multichannel waveguide grating filters. *Opto-Electron Sci* **3**, 240003 (2024).
19. Zhang YN, Liu YX, Shi BF et al. Lateral offset single-mode fiber-based Fabry–Perot interferometers with Vernier effect for hydrogen sensing. *Anal Chem* **95**, 872–880 (2023).
20. Luo JX, Liu S, Chen PJ et al. Highly sensitive hydrogen sensor based on an optical driven nanofilm resonator. *ACS Appl Mater Interfaces* **14**, 29357–29365 (2022).
21. Wang CQ, Han ZW, Wang CX et al. Highly sensitive fiber grating hydrogen sensor based on hydrogen-doped Pt/$WO_3$. *Sens Actuators B Chem* **404**, 135250 (2024).
22. Ye Z, Ruan HB, Hu XY et al. TBAOH intercalated $WO_3$ for high-performance optical fiber hydrogen sensor. *Int J Hydrogen Energy* **47**, 28204–28211 (2022).
23. Cai SS, Liu F, Wang RL et al. Narrow bandwidth fiber-optic spectral combs for renewable hydrogen detection. *Sci China Inf*

*Sci* **63**, 222401 (2020).
24. Gu FX, Wu GQ, Zeng HP. Hybrid photon–plasmon Mach–Zehnder interferometers for highly sensitive hydrogen sensing. *Nanoscale* **7**, 924–929 (2015).
25. Perrotton C, Westerwaal RJ, Javahiraly N et al. A reliable, sensitive and fast optical fiber hydrogen sensor based on surface plasmon resonance. *Opt Express* **21**, 382–390 (2013).
26. Nugroho FAA, Eklund R, Nilsson S et al. A fiber-optic nanoplasmonic hydrogen sensor *via* pattern-transfer of nanofabricated PdAu alloy nanostructures. *Nanoscale* **10**, 20533–20539 (2018).
27. Yun S, Oyama ST. Correlations in palladium membranes for hydrogen separation: a review. *J Memb Sci* **375**, 28–45 (2011).
28. Adhikari S, Efremova MV, Spaeth P et al. Single-particle photothermal circular dichroism and photothermal magnetic circular dichroism microscopy. *Nano Lett* **24**, 5093–5103 (2024).
29. Cui XM, Ruan QF, Zhuo XL et al. Photothermal nanomaterials: a powerful light-to-heat converter. *Chem Rev* **123**, 6891–6952 (2023).
30. Luo J, Wu QL, Zhou L et al. Plasmon-induced hot carrier dynamics and utilization. *Photonics Insights* **2**, R08 (2023).
31. Polley N, Sardar S, Werner P et al. Photothermomechanical nanopump: a flow-through plasmonic sensor at the fiber tip. *ACS Nano* **17**, 1403–1413 (2023).
32. Stewart JW, Nebabu T, Mikkelsen MH. Control of nanoscale heat generation with lithography-free metasurface absorbers. *Nano Lett* **22**, 5151–5157 (2022).
33. Wu HT, Chen PW, Zhan XD et al. Marriage of a dual-plasmonic interface and optical microfiber for NIR-II cancer theranostics. *Adv Mater* **36**, 2310571 (2024).
34. Ye Z, Li Z, Dai JX et al. Hydrogen sensing performance investigations with optical heating and sensing element surface modification. *Int J Hydrogen Energy* **46**, 1411–1419 (2021).
35. Zhang XP, Li XT, Zhang XH et al. Photothermal-assisted hydrogen permeation enhancement. *Sens Actuators B Chem* **365**, 131935 (2022).
36. Kaliteevski M, Iorsh I, Brand S et al. Tamm plasmon-polaritons: possible electromagnetic states at the interface of a metal and a dielectric Bragg mirror. *Phys Rev B* **76**, 165415 (2007).
37. Lundt N, Klembt S, Cherotchenko E et al. Room-temperature Tamm-plasmon exciton-polaritons with a $WSe_2$ monolayer. *Nat Commun* **7**, 13328 (2016).
38. Hu MY, Zhang Y, Jiang X et al. Double-bowl state in photonic Dirac nodal line semimetal. *Light Sci Appl* **10**, 170 (2021).
39. Kar C, Jena S, Udupa DV et al. Tamm plasmon polariton in planar structures: a brief overview and applications. *Opt Laser Technol* **159**, 108928 (2023).
40. Normani S, Bertolotti P, Bisio F et al. Tamm plasmon resonance as optical fingerprint of silver/bacteria interaction. *ACS Appl Mater Interfaces* **15**, 27750–27758 (2023).
41. Sreekanth KV, Perumal J, Dinish US et al. Tunable Tamm plasmon cavity as a scalable biosensing platform for surface enhanced resonance Raman spectroscopy. *Nat Commun* **14**, 7085 (2023).
42. He MZ, Nolen JR, Nordlander J et al. Coupled Tamm phonon and plasmon polaritons for designer planar multiresonance absorbers. *Adv Mater* **35**, 2209909 (2023).
43. Wang ZY, Ho YL, Cao T et al. High-Q and tailorable fano resonances in a one-dimensional metal-optical Tamm state structure: from a narrowband perfect absorber to a narrowband perfect reflector. *Adv Funct Mater* **31**, 2102183 (2021).
44. Lu H, Shi SH, Li DK et al. Strong self-enhancement of optical nonlinearity in a topological insulator with generation of Tamm state. *Laser Photonics Rev* **17**, 2300269 (2023).
45. Ko JH, Seo DH, Jeong HH et al. Sub-1-volt electrically programmable optical modulator based on active Tamm plasmon. *Adv Mater* **36**, 2310556 (2024).
46. Zhang KH, Chen ZY, Li HJ et al. A dual-band hydrogen sensor based on Tamm plasmon polaritons. *Phys Chem Chem Phys* **25**, 20697–20705 (2023).
47. Palm KJ, Murray JB, Narayan TC et al. Dynamic optical properties of metal hydrides. *ACS Photonics* **5**, 4677–4686 (2018).
48. Brovelli LR, Keller U. Simple analytical expressions for the reflectivity and the penetration depth of a Bragg mirror between arbitrary media. *Opt Commun* **116**, 343–350 (1995).
49. Adams M, Cemlyn B, Henning I et al. Model for confined Tamm plasmon devices. *J Opt Soc Am B* **36**, 125–130 (2019).
50. Peleg M, Normand MD, Corradini MG. The Arrhenius equation revisited. *Crit Rev Food Sci Nutr* **52**, 830–851 (2012).
51. Chen X, Chen YT, Yan M et al. Nanosecond photothermal effects in plasmonic nanostructures. *ACS Nano* **6**, 2550–2557 (2012).

## Acknowledgements

We are grateful for financial supports from National Key Research and Development Program of China (2023YFB3209500), National Natural Science Foundation of China (NSFC) (12274052 and 62171076), Fundamental Research Funds for the Central Universities (DUT24ZD203), Bolian Research Funds of Dalian Maritime University and Fundamental Research Funds for the Central Universities (3132024605). The authors acknowledge the assistance of Dr. Zhiguang Sun from the DUT Instrumental Analysis Center, as well as Mr. Qinhe Meng from Guide Sensmart and Beijing Shenzhou Jice Technology Co., Ltd., for their support in conducting the infrared thermal imaging tests.

## Author contributions

Xinran Wei conducted the numerical simulations, performed experimental measurements, and prepared the initial draft. Xuhui Zhang helped with the experimental measurement. Rui Li, Haonan Wei, Yijin He and Lanlan Shen assisted in data and results analysis. Yuzhang Liang, Ting Xu, Yurui Fang, and Wei Peng helped with theoretical analysis and supervised the project. Yuzhang Liang and Ting Xu supervised the manuscript writing. All authors participated in the discussion and confirmed the final manuscript.

## Competing interests

The authors declare no competing financial interests.

## Supplementary information

Supplementary information for this paper is available at https://doi.org/10.29026/oes.2025.240029